Catalysis Science & Technology

ROYAL SOCIETY OF CHEMISTRY

PAPER

View Article Online
View Journal | View Issue

Cite this: *Catal. Sci. Technol.*, 2026, **16**, 628

High-performance photocatalytic PSF/ZnO–GO membranes for the removal of pharmaceuticals and proteins from wastewater

Zouhair Salah,[a] Hajer Aloulou,[ad] Saurav Bhattacharyya,[be] Veronica Cozzolino,[bc] Catia Algieri,*[b] Sudip Chakraborty,[c] Vincenza Calabrò[c] and Raja Ben Amar*[a]

Received 5th August 2025,
Accepted 30th November 2025

DOI: 10.1039/d5cy00959f

rsc.li/catalysis

Effluents from the pharmaceutical industry pose significant environmental threats due to their complex and recalcitrant nature, including low biodegradability, high organic load, and the presence of emerging contaminants such as pharmaceutical residues. In this study, polysulfone (PSF) ultrafiltration membranes were modified with zinc oxide–graphene oxide (ZnO–GO) nanocomposites at varying loadings (0.6 and 1.2 wt%) *via* the phase inversion method to enhance their separation efficiency and photocatalytic performance. Physicochemical characterization was performed using scanning electron microscopy (SEM), energy-dispersive X-ray spectroscopy (EDXS), Fourier transform infrared spectroscopy (FTIR), contact angle analysis, and mechanical strength tests. The photocatalytic performance of the membranes was evaluated through the degradation of diclofenac (DCF), a model pharmaceutical contaminant, under UV irradiation (24 W) at an operating pressure of 3 bar. The membrane incorporating 0.6 wt% ZnO–GO exhibited the best overall performance, achieving a high-water flux of 19.12 L m^{-2} h^{-1} bar^{-1} and an 80% DCF removal efficiency. Furthermore, antifouling evaluation using bovine serum albumin (BSA) demonstrated a rejection rate of 91% and a flux recovery ratio (FRR) exceeding 86%, indicating strong resistance to fouling. These results demonstrate the potential of PSF/ZnO–GO nanocomposite membranes as high-performance, multifunctional systems for the advanced treatment of pharmaceutical wastewater, combining efficient filtration with photocatalytic degradation capabilities.

Introduction

Water contamination has become a major environmental issue, presenting considerable risks to human health and ecosystem stability.[1] These contaminants represent a serious threat to the survival of aquatic life and other living organisms.[2] Among the pollutants, pharmaceutical contaminants are one of the main worrying classes of emerging contaminants discharged in water, mainly from pharmaceutical plants.[3] A significant number of these pollutants originate from sources like biomedical waste from hospitals, human excreta, livestock vaccines, and veterinary medicine.[4] DCF is one of the most used anti-inflammatory drugs, and so it is frequently detected in aqueous effluents.[5] Drug contamination in the hydrosphere has impacted a wide range of aquatic species in various ways, such as by causing irregular behavior and reproduction, abnormal development, and a lack of metamorphosis.[6] In addition, serious health issues can develop in humans who have consumed large amounts of Pharmaceutical and Personal Care products (PPCPs) contaminated water over extended periods.

In previous studies, several methods have been used to remove non-steroidal anti-inflammatory drugs from aqueous solutions, including advanced oxidation processes,[7] photocatalysis, biological treatment, ion exchange removal, adsorption, and membrane separation.[8,9] As a result, photocatalytic technology has garnered increasing attention as an alternative treatment strategy, owing to its environmental compatibility, cost-effectiveness, and high degradation efficiency.[10] A variety of photocatalysts, such as TiO_2,[11] ZnO,[12] Ag, and CdS, have been successfully employed for wastewater treatment. ZnO, in particular, has attracted interest due to its notable chemical stability, hydrophilicity,[13] low toxicity, and relatively low production cost. However, ZnO's photocatalytic performance is hindered by the high recombination rate of photogenerated charge carriers and its

---

[a] *Research Unit 'Advanced Technologies for Environment and Smart Cities', Faculty of Sciences of Sfax, University of Sfax, Tunisia. E-mail: raja.benamar@fss.usf.tn*
[b] *Institute on Membrane Technology, National Research Council of Italy (ITM-CNR), Cubo 17C, Via Pietro Bucci, Rende 87036, Italy. E-mail: c.algieri@itm.cnr.it*
[c] *Department of DIMES, University of Calabria, Via Pietro Bucci, Cubo 42A, Rende 87036, Italy*
[d] *Department of Chemical, Preparatory Institute for Engineering Studies of Gabes, University of Gabes, Gabes 6029, Tunisia*
[e] *Department of DIBEST, University of Calabria, Via Pietro Bucci, Rende 87036, Italy*

wide bandgap (3.2 eV).[14] Various modification strategies, including doping, heterojunction formation with other semiconductors, and incorporation with noble metal nanoparticles, have been explored to enhance ZnO's photocatalytic efficiency. Among these, hybridization with carbon-based nanomaterials, such as GO and reduced graphene oxide (rGO), has emerged as a promising approach due to their high specific surface area, tunable electronic properties, and excellent charge transport capabilities.[15] Additionally, GO contains abundant oxygen-containing functional groups (such as carboxyl, hydroxyl, carbonyl, and epoxy groups), which enhance its dispersion in aqueous media and provide active sites for the attachment of ZnO nanoparticles.[16] Although numerous studies have examined photocatalytic degradation of pharmaceuticals, including Non-Steroidal Anti-Inflammatory Drugs (NSAIDs), using various treatment methods; however, the integration of photocatalysis with membrane systems remains insufficiently explored. In fact, PSF/ZnO, PSF/GO, and ZnO–GO membranes have been reported, most existing work focuses on standalone photocatalysts or general membrane improvements, with limited attention to their combined photocatalytic–filtration performance for NSAID removal. Furthermore, despite the promising properties of ZnO–GO composites (such as improved charge separation, enhanced surface functionality, and better dispersibility due to GO's oxygen-containing groups), their incorporation into PSF membranes and the resulting interfacial interactions affecting membrane structure and performance have not been thoroughly optimized. Addressing these gaps, this study provides a comparative evaluation of PSF/ZnO, PSF/GO, and PSF/ZnO–GO membranes specifically for NSAID degradation, simultaneously assessing photocatalytic activity and membrane performance while elucidating the synergistic effects introduced by the ZnO–GO network within the PSF matrix. These contributions collectively distinguish the present work and establish its novelty relative to existing literature.

In recent years, photocatalytic membrane reactors have gained significant interest in water treatment applications due to the integration of membrane filtration with photocatalytic degradation. The membrane loaded with photocatalytic nanoparticles (NPs) exhibits higher water permeability, improved fouling property, and enhanced solute rejection.[17] In addition, the NPs immobilization within the membrane matrix facilitates their separation, permits their recovery and reuse.[18] Despite these benefits, ZnO-based membranes are often limited by the agglomeration of ZnO nanoparticles, leading to uneven dispersion and reduced performance.[19] On the other hand, pristine GO membranes have had minimal effectiveness in desalination. Another disadvantage of this technology is that GO membranes are unstable, especially in humid conditions. To address these limitations, GO membranes have been supplemented with organic and inorganic compounds. GO/ZnO composite membranes exhibit five times more water permeability than pristine GO membranes, while maintaining similar rejection efficacy. Additionally, including ZnO nanoparticles into the GO membrane provides microbicidal capabilities, lowering the possibility of biofouling.[20] To overcome this limit, GO has been proposed as an ideal support material to improve nanoparticle dispersion and enhance membrane activity.[21] Several studies have demonstrated that polymeric membranes modified with rGO/GO–ZnO nanocomposites exhibit enhanced properties, including increased pure water flux, improved antifouling resistance, higher solute rejection, and greater photocatalytic degradation efficiency.[15] For example, Kusworo *et al.* reported that ZnO-modified membranes exhibited enhanced water uptake, hydrophilicity, flux recovery ratio, and antifouling property.[22] Similarly, Nasrollahi *et al.* reported a significant increase in the permeate flux and a notable reduction in the irreversible resistance for ZnO-modified PES membranes.[23] Additionally, Yu *et al.* demonstrated that ZnO incorporation into PVDF membranes maintained a steady flux with 100% recovery.[24] However, despite these promising advancements, challenges related to nanoparticle dispersion and long-term membrane stability remain to be addressed.

In this work, we introduce PSF ultrafiltration membranes modified with ZnO–GO nanocomposites, designed to simultaneously enhance water filtration efficiency and photocatalytic degradation of pharmaceutical contaminants. Unlike previous studies that examine ZnO–carbon hybrids primarily as standalone photocatalysts, our study demonstrates their integration into a membrane matrix to create a multifunctional system capable of both high-flux filtration and effective degradation of recalcitrant pollutants such as diclofenac.

In particular, in this study, a controlled hydrothermal method was employed to synthesize ZnO–GO nanocomposite photocatalyst. Furthermore, the fabrication of photocatalytic membranes based on PSF and ZnO–GO was achieved *via* the phase inversion method. The hydrophilicity of the membranes was assessed through water contact angle measurements, while their antifouling performance was evaluated by BSA rejection tests and FRR calculation. Furthermore, the chemical and mechanical properties of the membranes and their photocatalytic degradation of DCF under UV irradiation were thoroughly analyzed.

Experimental

Materials

PSF (molecular weight of 22 000 g mol^{-1}), zinc oxide nanopowder (particle size <100 nm), and zinc acetate dihydrate (Zn $(CH_3COO)_2 \cdot 2H_2O$, molecular weight of 219.5 g mol^{-1}) were supplied from Sigma-Aldrich. *N*-Methyl-2-pyrrolidone (NMP, 99.7%) was purchased from Merck (Germany) and used without purification as a solvent for the membrane preparation. Sodium hydroxide (NaOH) and ethanol (C_2H_5OH) were also purchased from Sigma-Aldrich. The diclofenac (DCF, $C_{14}H_{10}Cl_2NNaO_2$) was furnished by Sigma-Aldrich.

ZnO–GO nanocomposite preparation

GO nanoparticles, prepared from graphite material *via* the Modified Hummer,[25] were used for the preparation of ZnO–GO nanocomposites. In particular, ZnO–GO nanocomposites were prepared by a hydrothermal method. In this experiment, 20 mg of Zn $(CH_3COO)_2\cdot 2H_2O$ was dissolved in 30 mL of deionized water.[26] Subsequently, the solution was added to 25 mL containing 100 mg of GO and stirred for 15 minutes to form a homogeneous suspension. After, 30 mL NaOH solution (0.2 M) was added to the suspension and stirred for 60 min. Then, the resulting slurry was transferred into a 200 mL Teflon-lined stainless-steel autoclave that was placed in an oven and maintained at 120 °C for 10 hours. The sample was allowed to cool naturally in the oven, resulting in the formation of black ZnO–GO nanocomposites. The black precipitate was separated from the solution by centrifugation. The collected material was then dried at 80 °C and stored.

PSF/ZnO–GO membrane preparation

The mixed matrix membranes (MMMs) were prepared using the phase inversion method.[27] First, PSF polymer, ZnO, and ZnO–GO nanocomposites were dried overnight in an oven at 100 °C. The pristine PSF membrane was made by dissolving PSF in NMP (13 wt% of PSF). The polymer solution was stirred for 24 hours. The solution was cast using an automated casting machine (POROMETER MEMCAST, Netherlands) at a speed of 3 mm s^{-1} and 25 °C.

Following the method described previously, Mixed matrix membrane (MMMs) was synthesized by incorporating ZnO–GO (M_{ZG1} et M_{ZG2}) and ZnO (M_{Z1} et M_{Z2}) nanoparticles (between 0.6 wt% and 1.2 wt%) into the PSF solution. All membranes were initially air-dried and subsequently oven-dried at 60 °C for 24 hours. The compositions of the membranes are summarized in Table 1.

ZnO/GO and mixed matrix membranes characterization

The morphology of the ZnO–GO nanocomposites and MMMs was analyzed using a scanning electron microscope (SEM, Cambridge Zeiss LEO 400) and energy-dispersive X-ray spectroscopy (EDXS) with an accelerating voltage of 15 kV, performed on a ZEISS Crossbeam 350 UHR-SEM instrument.

Table 1 The casting solution compositions of the prepared membranes

Membrane	PSF (wt%)	ZnO (wt%)	ZnO–GO (wt%)	NMP (wt%)
PSF pristine	13	0	0	87
M_{Z1}	13	0.6	—	86.4
M_{Z2}	13	1.2	—	85.8
M_{ZG1}	13	—	0.6	86.4
M_{ZG2}	13	—	1.2	85.8

Functional groups present on ZnO–GO and MMMs were investigated using Fourier transform infrared spectroscopy (Spectrum Two FT-IR Spectrometer, Perkin–Elmer).

The structural properties of the ZnO–GO were also analyzed using X-ray diffraction (XRD) with a Rigaku MiniFlex 600 diffractometer (Japan) and CuKα radiation (λ = 1.5406 Å), operated at 40 kV and 20 mA. The XRD patterns were recorded in the 2θ range from 5° to 70°, with a step size of 0.02° and a scanning rate of 1° min^{-1}. The optical properties of the materials and the degradation rate of DCF were examined using a UV–visible spectrometer (Perkin–Elmer UV/vis lambda 365).

UV–visible diffuse reflectance spectroscopy (UV–vis DRS) was performed to investigate the optical properties of the ZnO–GO nanocomposite. The spectrum shows strong absorption in the UV region, with a clear absorption edge around 390 nm, which is typical for pure ZnO.[28] The optical band gap energy (E_g) can be estimated using eqn (1):

$$E_g = \frac{h_c}{\lambda} \tag{1}$$

where h is Planck's constant (6.626×10^{-34} J s), c is the speed of light (3.0×10^8 m s^{-1}), and λ is the wavelength at the absorption edge (in meters). For a more accurate estimation of the optical band gap, a Tauc plot was constructed using the Kubelka–Munk function, defined as (eqn (2)):

$$F(R) = \frac{(1-R)^2}{2R} \tag{2}$$

where R is the reflectance. Assuming a direct allowed electronic transition (as in the case of ZnO), the Tauc relation is given by eqn (3):

$$(F(R)h_v)^2 \propto (h_v - E_g) \tag{3}$$

Water contact angles for MMMs were evaluated by using a CAM 200 contact angle meter (KSV Instruments LTD, Helsinki, Finland). A drop (5 μL) of ultrapure water using an automatic micro-syringe was deposited on the smooth surface of the membranes. Four measurements were performed for each sample, and the standard deviations were calculated.

The mechanical properties of the membranes were evaluated utilizing a testing machine (Zwick/Roell, BTC-FR2.5TN.D09, Germany), considering a tensile speed of 10 mm min^{-1} and a 25 mm clamping distance at ambient temperature. For each sample, the measurement was repeated at least 5 times to minimize the error.

To evaluate the effect of nanoparticles on membrane structure, porosity was measured using the gravimetric method. Initially, the membranes were dried at 50 °C for 24 hours. Each membrane was then cut into five small pieces (1 cm × 1 cm) and weighed. The samples were immersed in distilled water at 25 °C for 24 hours. After immersion, surface water was carefully removed using a paper filter, and the membranes were reweighed. The overall porosity (ε)

was calculated using the gravimetric method, as defined by eqn (4).

$$\varepsilon = \frac{W_1 - W_2}{A \times l\ d_{\mathrm{w}}} \times 100 \tag{4}$$

where w_1 is the weight of the wet membrane, w_2 is the weight of the dry membrane; A is the membrane effective area (m^2), d_w is the water density (998 kg m^{-3}), and l is the membrane thickness (m). All tests were replicated three times, and the mean values were taken into account. In addition, to determine the membrane mean pore radius (r_m), the Guerout–Elford–Ferry equation (eqn (5)) is based on the pure water flux and porosity data (see eqn (4)).

$$r_{\mathrm{m}} = \sqrt{\frac{(2.9 - 1.75\varepsilon) \times 8\eta l Q}{\varepsilon \times A \times \Delta P}} \tag{5}$$

where r_m is the mean pore radius (m), η is the water viscosity (8.9×10^{-4} Pas), l is the membrane thickness (m) measured by using a micrometer, Q is the volume of the permeate water per unit time ($m^3\ s^{-1}$), A is the effective area of the membrane (m^2) and ΔP is the operational pressure (Pa).

The chemical stability of the synthesized membranes was evaluated by measuring weight loss over time after immersion in acidic (HNO_3, 0.2 M, pH = 1) and alkaline (NaOH, 0.5 M, pH = 12) solutions at room temperature for three days.

Pure water flux and photocatalytic tests

A dead-end membrane module was used for measuring the pure water flux (J), applying a transmembrane pressure (ΔP = 1–3 bar). The permeate flux was calculated using eqn (6).

$$J = \frac{V}{A \times t} \tag{6}$$

where J is the permeating flux through the membrane, V is the permeate volume collected during the time t, and A is the membrane area (38.5 cm^2). The permeability was determined by plotting the slope of the permeate flux *versus* ΔP according to Darcy's law.

The photocatalytic activity was evaluated by monitoring the degradation of an aqueous DCF solution using ZnO–GO nanocomposites, commercial ZnO nanoparticles, and the fabricated MMMs (PSF–ZnO–GO and PSF-ZnO).

The photocatalytic activity of the synthesized ZnO–GO nanocomposite was assessed in a batch-type photoreactor system under UV irradiation (Fig. 1a). A quartz glass beaker (250 mL capacity) was used as the reaction vessel and placed inside a black box to prevent interference from ambient light. A UV lamp (365 nm, 24 W) was positioned 10 cm above the solution surface to provide consistent and direct irradiation during the photocatalysis process. A DCF solution (V = 100 mL) with an initial concentration of 25 mg L^{-1} was added into the reactor. The ZnO–GO nanocomposite photocatalyst was added to the solution and dispersed *via* magnetic stirring. The suspension was first kept under dark conditions for 30 minutes to achieve adsorption–desorption equilibrium between the photocatalyst and DCF. After dark equilibration, the UV lamp was switched on to initiate photocatalytic degradation. During the reaction, the suspension was continuously stirred to maintain uniform dispersion and minimize mass transfer limitations. At regular time intervals, aliquots (3–5 mL) of the suspension were withdrawn, centrifuged for 10 minutes, and filtered using a syringe filter to remove photocatalyst particles.

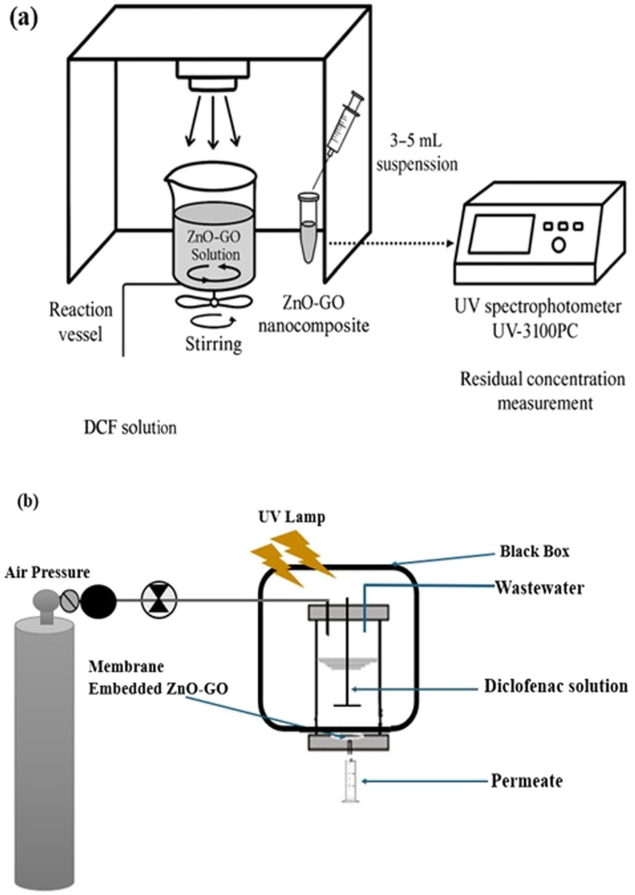

Fig. 1 Schema of: a) photocatalytic reactor and b) immobilized photocatalytic membrane reactor.

The photocatalytic efficiency of the prepared membranes was evaluated using a photocatalytic membrane reactor illustrated in Fig. 1b. A UV lamp with a power of 24 W and a wavelength of 365 nm was used to activate the photocatalytic species. The membrane was mounted in a dead-end ultrafiltration cell and exposed to UV irradiation. The distance between the UV lamp and the cell was approximately 10 cm. All experiments were conducted at a temperature of 30 °C under a transmembrane pressure of 3 bar. The photocatalysts were activated using a UV lamp. A solution of DCF with a concentration of 25 mg L^{-1} (V = 200 mL) was introduced into the membrane photoreactor.

The concentration of DCF was measured using a UV spectrophotometer (UV-3100PC Spectrophotometer, China) at an absorbance wavelength of 273 nm. The degradation efficiency (%) was calculated using the following eqn (7):

$$\text{Dégradation}\,(\%) = \frac{(C_0 - C_t)}{C_0} \times 100 \tag{7}$$

where C_0 is the initial DCF concentration (mg L^{-1}) and C_t is the DCF concentration at time t.

The Langmuir–Hinshelwood (LH) kinetic model is used to describe heterogeneous catalysis, particularly in surface reactions. The rate of reaction is influenced by the pollutant concentration, as described in eqn (8):

$$r = \frac{\mathrm{d}C}{\mathrm{d}t} = \frac{-kKC}{1 + KC} \tag{8}$$

where r represents the reaction rate, C denotes the concentration of dye in the solution, t stands for time, k represents the reaction constant, and K is he adsorption equilibrium factor for the pollutant on the photocatalyst's surface. By considering 'KC' to be negligible, the equation can be simplified as follows eqn (9):

$$\ln\left(\frac{C_0}{C_c}\right) = K't \tag{9}$$

where C_0 is the initial concentration, C is the concentration at time t. In addition, $K' = -kK$.

Antifouling studies

For the evaluation of fouling resistance, during the experiments with real photo-treated wastewater, three different flux steps were considered. In the first step, the pure water flux (J_W) was measured for 1 h at 3 bar. Then, 50 mg L^{-1} BSA solution, as a suitable fouling agent for rejection and antifouling tests, was fed into the filtration system, and the flux (J_P) was measured for another 1 h. In the final step, followed by BSA filtration, the fouled membrane was rinsed with deionized water, and the water flux (J_{WA}) of the membrane was measured for 1 h.

The fouling characteristic of the membranes was evaluated by calculating the Flux Recovery Ratio (FRR) using the following eqn (10):

$$\mathrm{FRR} = \frac{J_{WA}}{J_W} \times 100 \tag{10}$$

Results and discussions

ZnO–GO nanocomposite characterization

The morphology of ZnO, GO, and ZnO–GO was examined using scanning electron microscopy. The SEM image of GO (Fig. 2a) showed a characteristic wrinkled and crumpled sheet-like structure, indicating successful exfoliation and suggesting a high surface area and porosity. The layered structure improves interfacial interactions within composite materials. In contrast, the commercial ZnO, as shown in Fig. 2b, appeared as densely packed, aggregated particles with smooth surfaces and low porosity, typical of bulk ZnO and indicative of limited nanoscale features. The SEM analysis of the ZnO–GO nanocomposite (Fig. 2c) revealed a rougher, more heterogeneous surface texture, with ZnO nanoparticles evenly distributed on the GO sheets. This well-dispersed arrangement demonstrates strong interactions between ZnO and GO nanosheets, which can effectively prevent ZnO from agglomerating and increase the number of accessible active sites. This structure benefits photocatalytic performance and facilitates charge transfer in hybrid

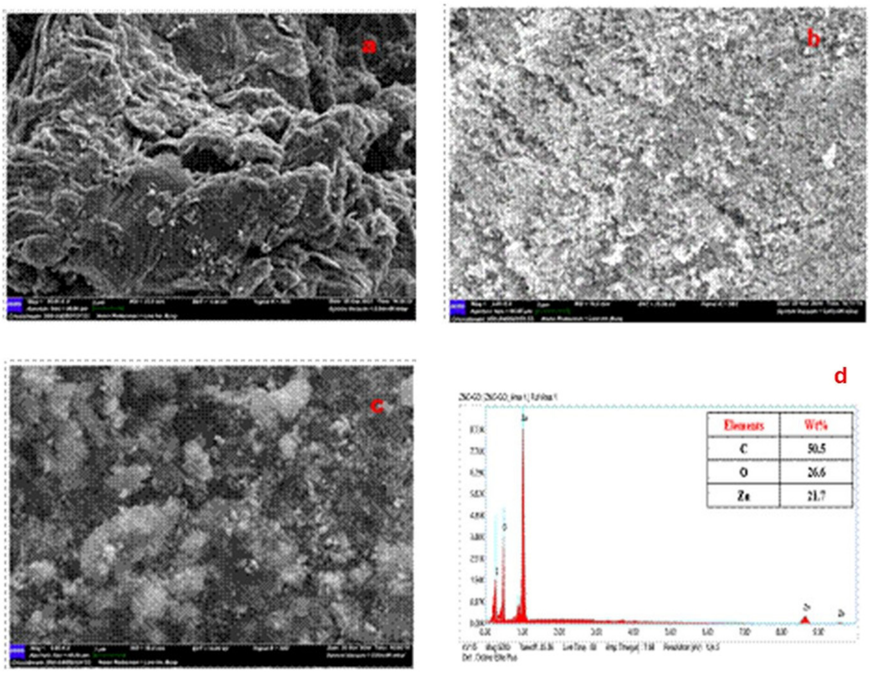

Fig. 2 SEM pictures of: a) GO nanosheets, b) commercial ZnO, and c) ZnO–GO nanocomposites. d) EDX spectrum of ZnO–GO nanocomposite.

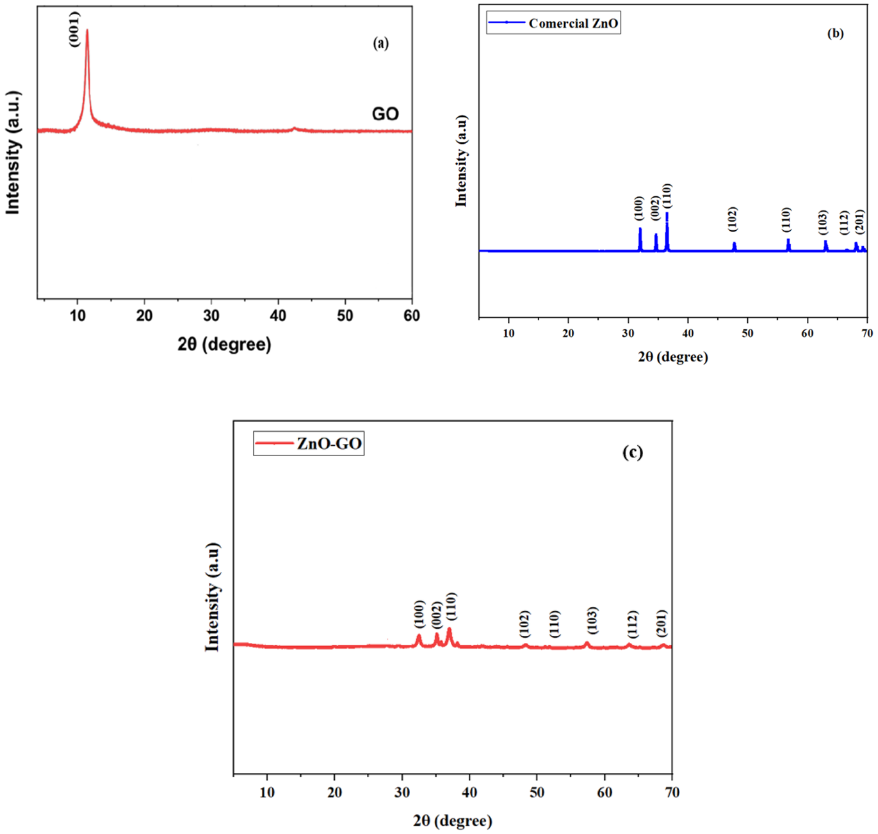

Fig. 3 XRD spectra of: a) GO nanosheets, b) commercial ZnO, and c) ZnO–GO nanoparticles.

materials. The EDX spectrum shown in Fig. 2d clearly displays three main elements: zinc (Zn), oxygen (O), and carbon (C). The peaks for Zn and O confirm the successful incorporation of ZnO nanoparticles into the composite, while the presence of C is due to the GO component.

The X-ray diffraction (XRD) analysis was performed to investigate the crystalline structure of the synthesized ZnO and ZnO–GO nanocomposites.

The GO spectrum exhibits a characteristic (001) diffraction peak at approximately 11.3°, as shown in Fig. 3, reflecting the layered structure and the presence of oxygen-containing functional groups characteristic of graphene oxide.[29] The commercial ZnO sample displays sharp and intense peaks at 2θ values of 31.8°, 34.4°, 36.3°, 47.5°, 56.6°, 62.9°, and 68.0°, corresponding to the (100), (002), (110), (102), (110), (103), and (112) planes, respectively, which match well with the hexagonal wurtzite structure of ZnO (JCPDS No. 36-1451).[30] These peaks confirm the high crystallinity and purity of the ZnO phase. The ZnO–GO nanocomposite retains all major diffraction peaks of ZnO, indicating that the crystalline structure of ZnO is preserved during composite formation. Notably, the disappearance or significant suppression of the GO (001) peak in the composite suggests successful exfoliation or partial reduction of GO, likely due to strong

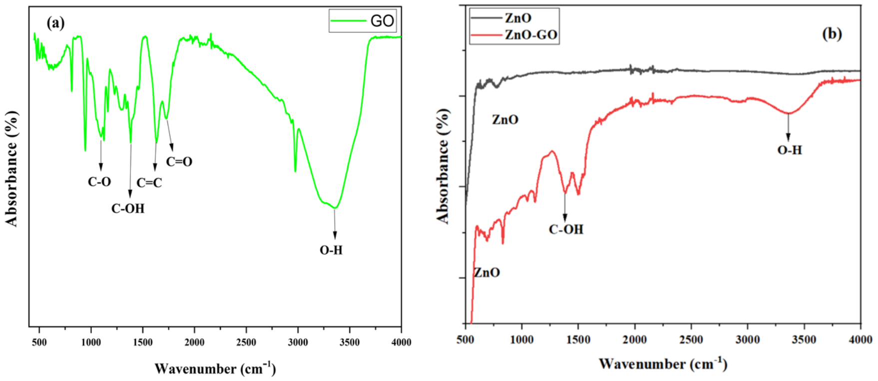

Fig. 4 FTIR spectra of a) GO and b) commercial ZnO and ZnO–GO nanoparticles.

interfacial interactions between ZnO and GO sheets during synthesis.[31] This change also implies a high degree of dispersion of GO within the ZnO matrix. Moreover, the absence of any additional peaks suggests no secondary phases were formed, confirming the effective integration of ZnO and GO without altering their primary structures. These results support the successful formation of a structurally intact ZnO–GO nanocomposite, which may exhibit enhanced physicochemical properties suitable for applications in photocatalysis, sensing, and environmental remediation.

FTIR analysis of the prepared nanoparticles was performed to evaluate the functional groups present in the nanomaterials (see Fig. 4). The ZnO spectrum displays peaks at 500 cm^{-1} and 750 cm^{-1} (as shown in Fig. 4b), which are in agreement with results reported in other studies.[32] Other researchers have reported that the peaks for ZnO appear between 400 cm^{-1} and 700 cm^{-1}.[33] In the spectrum of the GO nanosheet (Fig. 4a), the peak at 3362 cm^{-1} is observed, corresponding to the O–H stretching vibration, occurring from hydroxyl and adsorbed water molecules on the GO surface. These peaks confirm the successful oxidation of graphite into GO, consistent with previously reported studies.[34] Additionally, the peak at 1636 cm^{-1} is attributed to the stretching of aromatic C═C bonds. However, the peaks at 1727 cm^{-1} is attributed to the C═O stretching vibration of carbonyl or carboxyl groups present at the edges of GO sheets.[35] The nanocomposite ZnO–GO spectrum retains most of the characteristics of ZnO and GO; however, there are significant changes in pic intensity and slight shifts in position. More specifically, the intensity of images of functionally oxygenated groups (C–O and C–OH) increases in comparison to the GO peaks spectrum. This enhancement suggests strong interactions or a probable connection between ZnO nanoparticles and GO oxygenated groups. Furthermore, a slight decrease in the pic of oxidation of Zn–O is seen, indicating a chemical link or coordination between Zn atoms and functional groups of GO (such as –OH or –COOH).[36] These interactions reveal that ZnO nanoparticles adhere to the GO surface *via* covalent or electrostatic interactions, resulting in the effective development of a ZnO–GO nanocomposite. The reduction and intensification of composite spectra in comparison to those of individual components confirm the finding that ZnO has been well integrated into GO.

The optical response of the ZnO–GO was determined using UV-vis diffuse reflectance spectroscopy (UV-vis DRS), and the results are displayed in Fig. 5a. The resultant GO–ZnO nanocomposite shows extended and strong photoresponse from the UV region and throughout the visible light region (between 250 and 400 nm).

As shown in Fig. 5b, the linear portion of the plot was extrapolated to the *x*-axis, yielding an estimated band gap of 2.93 eV. The observed band gap has a lower value compared to the pristine ZnO, which typically exhibits a band gap of about 3.3 eV.[37]

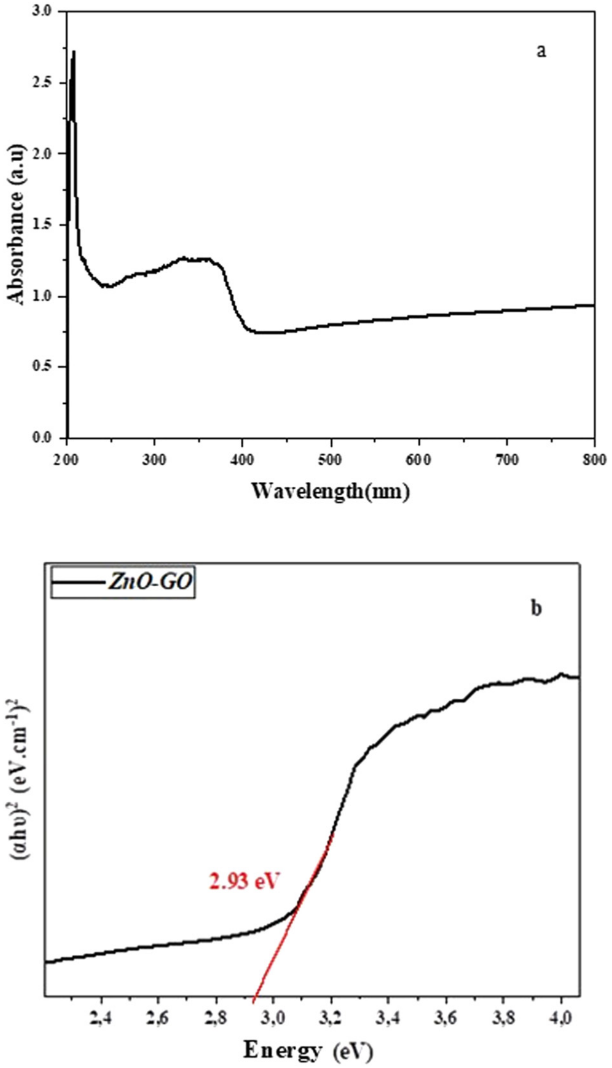

Fig. 5 (a) UV–visible DRS and (b) Tauc plot showing the energy band gap of ZnO–GO nanocomposite.

Similar reductions in band gap have been reported in other ZnO–GO systems. For instance, Khan *et al.* reported a band gap of 2.9 eV for ZnO-GO nanocomposites synthesized *via* sol–gel techniques.[38] Likewise, Ramesh and co-workers observed a slight shift to 2.95 eV and attributed it to electronic interactions at the ZnO–GO interface, which introduce mid-gap states or modify the conduction and valence bands.[39] This reduction in band gap is particularly significant for applications that require visible-light activity. The presence of GO not only enhances light absorption but also helps to avoid electron–hole recombination by acting as an electron acceptor, ultimately improving the overall performance of the nanocomposite.

Membranes characterization

SEM images of the surface and the cross-section of the prepared membranes are illustrated in Fig. 6. The fabricated membranes have an asymmetric structure consisting of a

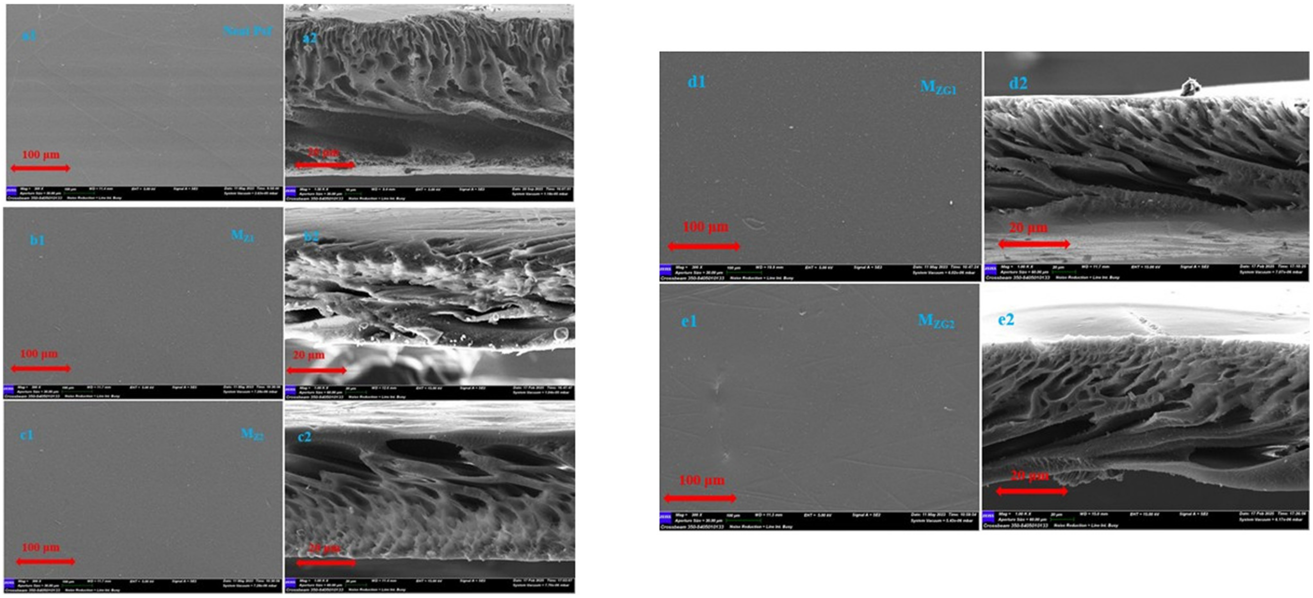

Fig. 6 SEM images of top view: a1) PSF, b1) M_{Z1}, c1) M_{Z2}, d1) M_{ZG1} and e1) M_{ZG2} and cross-section of a2) PSF, b2) M_{Z1}, c2) M_{Z2}, d2) M_{ZG1} and e2) M_{ZG2} samples.

dense skin layer and finger-like porous sublayer morphology. This kind of structure is commonly found in the prepared membrane by the inversion phase method.[40] It can be observed that neat PSF has finger-like microvoids, and so does the nano-ZnO incorporated into the membrane matrix. However, the finger-like voids of the MMM membranes are larger than those of the pristine membrane. The ZnO enhances the hydrophilicity of the doped solution. Due to its strong hydrophilic nature, nano ZnO facilitates faster solvent diffusion during phase inversion. The finger-like micro-void structure extends from the middle to the bottom of the membrane. As shown in Fig. 6, the nanoparticle ZnO distribution is localized on the surface of the membrane, and this is probably caused by the mixing process when the polymer solution is in contact with the non-solvent. During this process, the solvents migrate from the polymer solution phase to the non-solvent phase. The empty sites due to the solvent migration exiting the polymer matrix are replaced by non-solvent molecules, which depress the ZnO-nanoparticles towards the surface. This condition is advantageous in membrane fabrication because the addition of metal oxide filler will significantly increase the hydrophilicity of membrane surfaces.[41] The increase of membrane hydrophilicity improves the permeate flux performance and minimizes membrane fouling issues.[42] During filtration, water molecules pass through the membrane *via* non-clogged pores created by the interspace between nano-ZnO particles and polymer; thus, enhancing the permeate flux. There is a significant difference for the GO-incorporated membrane (Fig. 6d1 and e1) compared with those of pristine PSF and PSF–ZnO membranes. The finger-like structures of the PSF–ZnO and PSF/ZnO–GO are narrow, but they have high cell numbers.

The EDX analyses performed on the membrane cross-sections revealed an increased content of Zn in the MMMs membranes compared to the neat pristine PSF membrane, confirming the incorporation of nanocomposites into the polymeric membrane structure (see Fig. 7a1–a4). Furthermore, it was observed that the weight% of Zn increased proportionally with the ZnO–GO photocatalyst embedded in the nanocomposite membranes.

FTIR study. The FTIR spectrum of the pristine membrane, as illustrated in Fig. 8, exhibited a band at 1154 cm^{-1} owing to the stretching vibration between the oxygen atoms and aromatic rings.[43] The peaks at 1242 $cm^{-1}$and 1154 cm^{-1} were attributed to the asymmetric and symmetric stretching of the O=S=O group, respectively.[44] Peaks observed at 1311 cm^{-1} and 1587 cm^{-1} correspond to the symmetric stretching of the C=C bond and the stretching vibration of the C–O bond, respectively.[45] New peaks for the PSF/ZnO–GO membranes at 3200–3500 cm^{-1} confirmed the presence of the OH stretching and OH bonding,[46] resulting from the addition of GO nanoparticles. These results indicated the successful incorporation of ZnO–GO nanocomposite into the membrane. These hydrophilic functional groups enhance the hydrophilicity of the PSF/ZnO–GO membrane.

The mechanical properties of the membranes are strongly influenced by both the nanoparticle content and their dispersion within the PSF matrix. At low loadings (0.6 wt% ZnO in M_{Z1} and 0.6 wt% ZnO–GO in M_{ZG1}), the nanoparticles are well-dispersed and act as reinforcing agents, enhancing stress transfer between the polymer chains and the fillers. This results in increased tensile strength and Young's modulus compared to the neat PSF membrane (Table 2). The ZnO–GO hybrid, in particular, provides a synergistic effect: GO nanosheets offer high surface area and functional groups

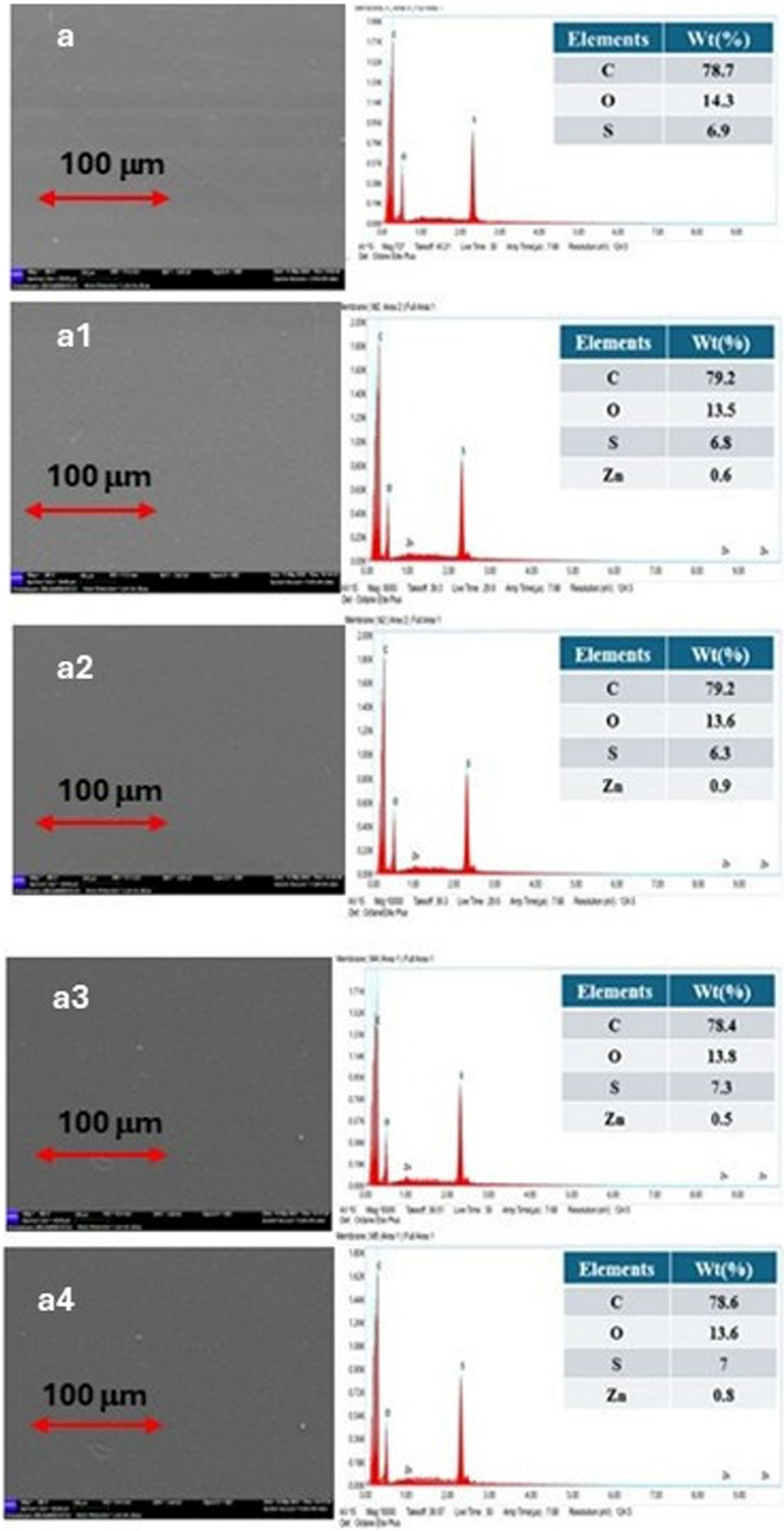

a

Elements	Wt(%)
C	78.7
O	14.3
S	6.9

a1

Elements	Wt(%)
C	79.2
O	13.5
S	6.8
Zn	0.6

a2

Elements	Wt(%)
C	79.2
O	13.6
S	6.3
Zn	0.9

a3

Elements	Wt(%)
C	78.4
O	13.8
S	7.3
Zn	0.5

a4

Elements	Wt(%)
C	78.6
O	13.6
S	7
Zn	0.8

Fig. 7 Elemental microanalyses and EDX pattern of the different samples: (a) neat PSF membrane, (a_1) M_{Z1}, (a_2) M_{Z2}, (a_3) M_{ZG1}, (a_4) M_{ZG2}.

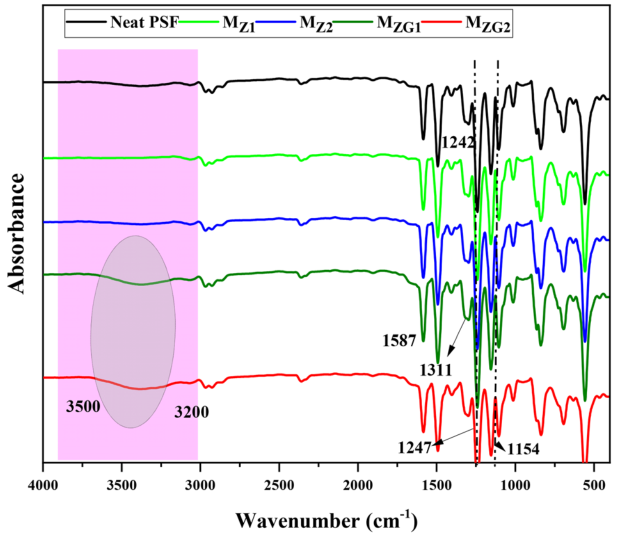

Fig. 8 FTIR spectra of the pristine membrane (neat PSF) and the prepared MMMs membranes.

Table 2 Tensile strength, tensile strain at break, and Young's module of the different prepared membranes

Membrane's types	Tensile strain at break (%)	Tensile strength (MPa)	Young's module (MPa)
Neat PSF	21.2 ± 1.18	3.97 ± 1.00	93.65 ± 11.04
M_{Z1}	17.42 ± 1.17	4.61 ± 1.08	136 ± 10.02
M_{Z2}	15.54 ± 1.35	3.44 ± 1.11	97.64 ± 4.02
M_{ZG1}	24.4 ± 1.2	4.8 ± 1.05	154.52 ± 11.16
M_{ZG2}	21.2 ± 1.08	3.5 ± 1.05	91.62 ± 4.05

that strengthen interfacial bonding, while ZnO nanoparticles contribute stiffness, collectively improving membrane robustness. These results are also confirmed by the SEM analyses. In contrast, at higher loadings (1.2 wt% ZnO or ZnO–GO in M_{Z2} and M_{ZG2}), nanoparticle aggregation occurs, creating stress concentration points that weaken the polymer network and reduce mechanical performance.[47] At higher nanoparticle loadings (1.2 wt% in M_{Z2} and M_{ZG2}), SEM and porosity analyses indicate aggregation and hindered macrovoid formation, which lead to irregular structures and reduced effective polymer–nanoparticle interactions. As a result, mechanical properties decrease despite similar or slightly increased porosity. Therefore, the mechanical strength is primarily controlled by nanoparticle dispersion and interfacial interactions rather than porosity alone, highlighting that an optimal balance of low nanoparticle loading and uniform distribution is critical for enhancing both structural and mechanical performance. These findings are consistent with recent studies highlighting the benefits of hybrid nanoparticles in enhancing both their dispersion and interfacial bonding within polymer matrices.[48]

The porosity and the mean pore radius of the MMMs membranes increased with the incorporation of different percentages of ZnO and ZnO–GO (see Table 3). The improved hydrophilicity of the prepared membrane, attributed to the hydrophilic functional groups that appeared on ZnO–GO nanocomposite material, would accelerate the membrane formation process by speeding up the demising rate between solvent and non-solvent and consequently increase the membrane porosity and mean pore radius.[49,50] However, a slight decrease in membrane porosity was observed at the highest ZnO–GO loading of 1.2 wt%. This behavior can be attributed to the increased viscosity of the membrane polymer solution caused by the high concentration of ZnO–GO nanocomposite material, which hindered the solvent-non-solvent exchange during phase inversion and slowed the membrane solidification process. As a result, the formation of macro-voids was limited, leading to a less porous membrane structure. Similarly, the mean pore radius increased from 16.71 nm for the PSF pristine membrane to 19.94 nm for M_{Z1} with incorporating 0.6 wt% ZnO and to 21.88 nm for M_{ZG1} with 0.6 wt% ZnO–GO. However, it decreased slightly when the nanoparticle loading was high at 1.2 wt% for M_{Z2} and M_{ZG2}. These results agree with the relationship between nanoparticle loading and membrane structural properties.

Table 3 Pore properties of the fabricated membranes

Membranes types	Porosity (%)	Mean pore radius r(nm)
Neat PSF	74	16.71 ± 0.61
M_{Z1}	80	19.94 ± 0.41
M_{Z2}	89	24.47 ± 0.51
M_{ZG1}	83	21.88 ± 0.035
M_{ZG2}	79	18.61 ± 0.055

The PSF membrane demonstrates excellent thermal stability, mechanical strength, and chemical resistance, but it is highly prone to fouling due to its inherent hydrophobicity. The addition of hydrophilic materials such as GO and ZnO nanoparticles enhances the membrane's hydrophilicity, improving water affinity, reducing fouling, and boosting

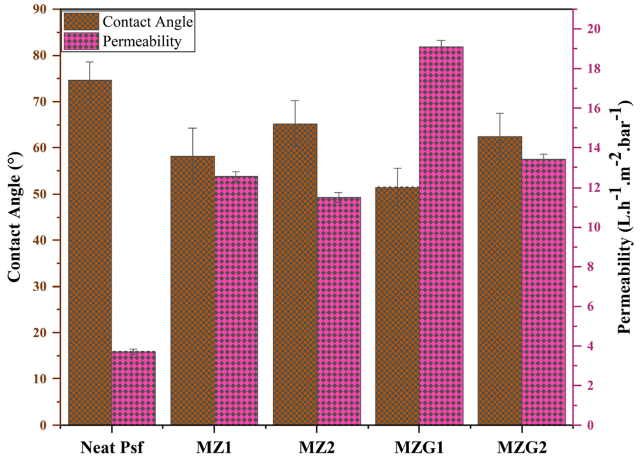

Fig. 9 Pure water permeability and water contact angle of the prepared membranes.

overall performance. In fact, a decrease in the water contact angle values was detected at low concentration (0.6 wt% %) of both ZnO and ZnO–GO, indicating enhanced hydrophilicity (see Fig. 9).[51] However, increasing the filler concentration from 0.6 wt% to 1.2 wt% caused a slight rise in the water contact angle due to cluster formation, indicating a decrease in surface hydrophilicity. The increased hydrophilicity also determined an increase in the water permeability. In fact, MMMs membranes embedded with ZnO and ZnO–GO nanoparticles exhibited higher permeability compared to the pristine one. In particular, incorporating ZnO–GO nanoparticles into the PSF matrix significantly enhances the membrane's water permeability through several synergistic effects.[52] Notably, incorporating ZnO–GO nanoparticles into the PSF matrix significantly improves water permeability through several synergistic effects. GO is rich in oxygen-containing functional groups (such as hydroxyl, epoxy, and carboxyl) while ZnO nanoparticles are inherently hydrophilic. Together, these components increase the overall membrane hydrophilicity, thereby enhancing water permeability and reducing fouling. These results are illustrated in Fig. 9. Potential leaching of ZnO or graphene oxide fragments during operation, particularly under UV irradiation and applied pressure, was carefully evaluated. Light scattering analysis of the collected permeate confirmed the absence of particulate leaching, indicating that the ZnO–GO nanocomposite remained stably immobilized on the membrane surface.

Chemical resistance

Chemical cleaning is a widely accepted method for minimizing flux decline and membrane fouling. Among the various cleaning techniques, it remains the most commonly used. Chemical cleaning is divided into acidic and alkaline cleaning. Acidic agents are utilized to eliminate inorganic deposits, while alkaline agents target organic contaminants, including microorganisms. However, chemical cleaning can significantly affect the physical and chemical properties of membranes, potentially damage the surface, and compromise their selectivity. To evaluate their stability under aggressive chemical environments, the stability of the prepared membranes was assessed under acid and alkaline conditions. The weight loss increased progressively throughout the experimental period (see Fig. 10). The best overall stability was observed for the M_{Z1} membrane, with weight losses of 0.45% in acidic medium and 1.2% in alkaline medium, followed by M_{ZG1}, which showed losses of 1.45% and 2.1% in acidic and alkaline media, respectively. In contrast, the M_{Z2} and M_{ZG2} membranes exhibited higher weight losses, 1.6% in acidic medium and 2.5% in alkaline medium for M_{Z2}, and 1.9% and 2.8%, respectively, for M_{ZG2}.

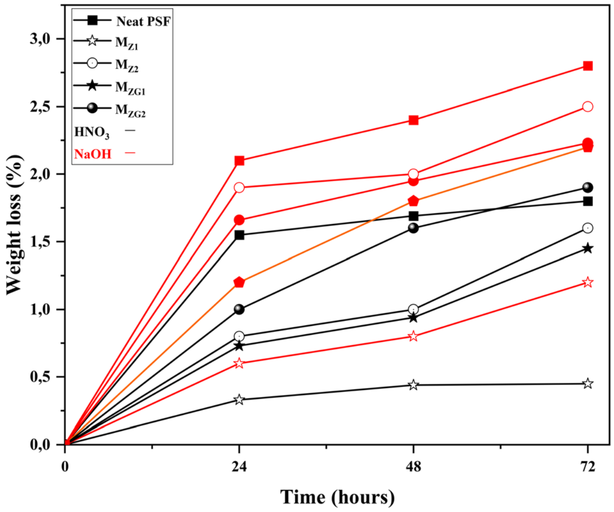

Fig. 10 Weight loss percentage *versus* time of the prepared membranes after immersion in HNO_3 (0.2 M) and NaOH (0.5 M) for 3 days.

Photocatalytic study

The results of the photocatalytic DCF degradation by considering ZnO–GO nanocomposite, ZnO nanoparticle, GO nanosheet, and photolysis (light exposure without catalyst) are reported in Fig. 11a. The used catalyst concentration was 0.6 g L^{-1}. The ZnO–GO nanocomposite exhibited the highest degradation efficiency, providing a DCF degradation approaching nearly zero within 180 minutes. The better performance of the nanocomposite material can be attributed to the synergistic effect between ZnO and GO. The ZnO nanoparticles are a well-known photocatalyst due to their ability to generate electron–hole (e–h) pairs under UV or visible light irradiation. However, they suffer from rapid recombination of these charge carriers.[53] GO, with its high surface area and excellent electron mobility, acts as an effective electron acceptor, reducing recombination and enhancing the formation of reactive oxygen species such as hydroxyl radicals (·OH) and superoxide anions ($\cdot O_2^-$).[54] These reactive species play a crucial role in breaking down organic pollutants. GO on its own displays minimal photocatalytic behavior, contributing primarily through adsorption and slight activation under light. In contrast, photolysis (light exposure without a catalyst) shows negligible degradation, confirming that light alone is insufficient to decompose the pollutant.[55] The photocatalytic performance of the various prepared membranes was also assessed, and the results are illustrated in Fig. 11b and c. The pristine membrane exhibits a very limited DCF degradation, with final removal efficiencies of 20% after 240 minutes. The presence of ZnO (M_{Z1} and M_{Z2} membranes) increased the DCF degradation. More pronounced improvement in degradation efficiency is observed with the M_{ZG1} sample; this membrane, containing 0.6 wt% of ZnO–GO, achieved the highest degradation rate (approximately 81%). However, the slight reduction in performance at higher ZnO–GO concentration (1.2 wt%) is attributed to the aggregation of nanoparticles within the membrane matrix, resulting in a reduction of catalytically active sites.[56] After about 150 minutes, the DCF removal

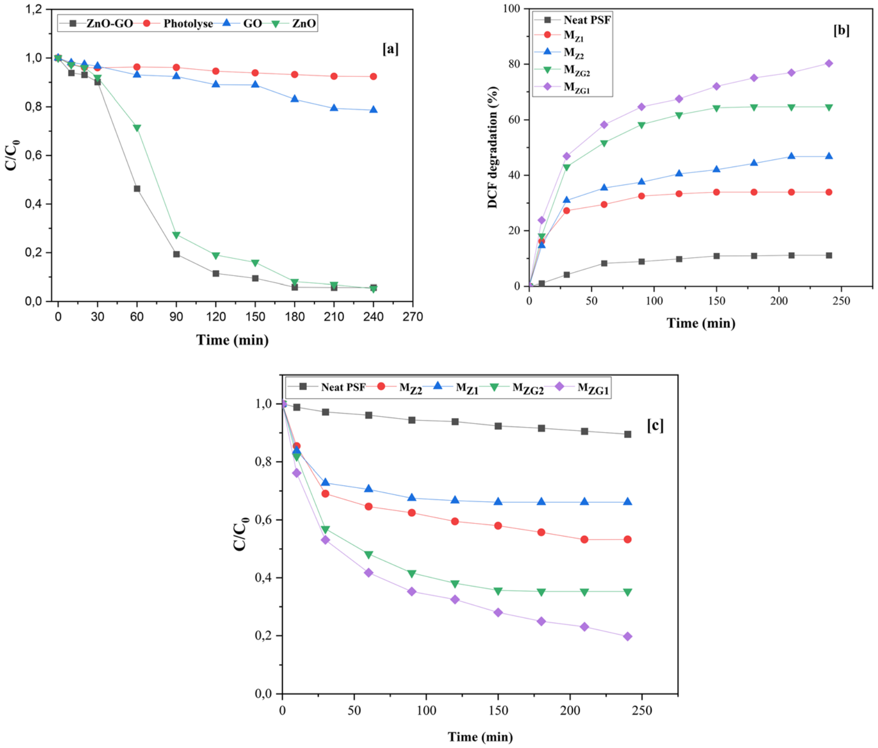

Fig. 11 (a) Photocatalytic degradation of DCF by GO, ZnO, and ZnO–GO nanoparticles. (b) and (c) removal of DCF by photocatalytic membranes.

reaches a plateau, due to the saturation of active sites. It is important to evidence that the membrane configuration provides several important practical advantages: it ensures continuous contact between pollutants and immobilized photocatalytic sites, enhances mass transfer of DCF to the active sites through convective flow, and, importantly, avoids the need for post-treatment separation of nanoparticles, which is a major limitation in conventional slurry-based photocatalysis. Therefore, while UV irradiation alone maximizes photocatalytic activity in dispersed nanoparticles, the pressure-driven photocatalytic membrane reactor offers a stable, reusable, and scalable approach for pollutant degradation, combining moderate photocatalytic efficiency with operational simplicity and catalyst retention.

The kinetic study for the DCF degradation demonstrated that the photodegradation process followed the first-order kinetic reaction (Fig. 12). The observed pseudo-first-order kinetics for DCF degradation likely result from a combination of photocatalytic reaction and adsorption. The high surface area and oxygen-containing functional groups of GO and ZnO–GO nanocomposites allow DCF molecules to adsorb onto the membrane or catalyst surface before degradation. This adsorption increases the local concentration of the pollutant near active sites, enhancing the apparent reaction rate and contributing to the pseudo-first-order behavior. In the membrane system, the well-dispersed ZnO–GO in MZG1 promotes efficient adsorption and photocatalytic conversion, leading to the highest rate constant, '*k*'. Concerning external mass-transfer limitations, the low nanoparticle loadings and the flow-through membrane design are expected to minimize diffusion constraints, as convective transport efficiently delivers DCF molecules to the catalytic sites. The plateau observed after 150 minutes likely reflects saturation of adsorption sites rather than mass-transfer limitations. Overall, adsorption plays a supporting role in the observed kinetics, while the membrane structure and hydrophilic properties help reduce external mass-transfer resistance.[57]

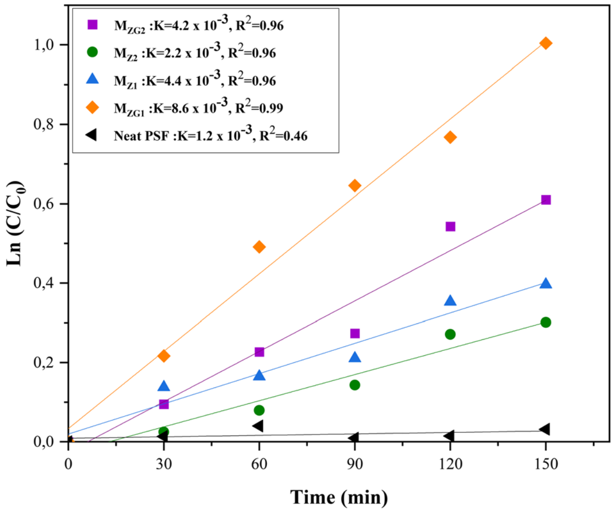

Fig. 12 Kinetic study results with the application of a first-order model for the DCF removal using the prepared membranes.

BSA resistance and antifouling characteristics of PSF/ZnO–GO nanocomposite membranes

Membrane fouling and flux reduction are significant challenges in membrane technology due to the build-up of solute particles during filtration. One effective approach to limit fouling is enhancing membrane hydrophilicity by adding hydrophilic fillers.[58] In this study, the incorporation of ZnO and ZnO–GO nanocomposite into the PSF membrane increased hydrophilicity and reduced fouling. The application of the manufactured membranes was performed for the filtration of the bovine serum albumin (BSA) solution as a fouling agent.[59] The flux recovery ratio demonstrated the efficacy of the composite membranes in the improvement of the BSA filtration performances.[60] An improvement in BSA rejection is obtained by adding the nanoparticles concentration in the PSF membrane, as shown in Fig. 13. The pristine PSF membrane exhibited a relatively low protein rejection of about 51%. This result is consistent with findings reported in the literature.[61] Higher BSA rejection (R = 91%) is obtained by using the membrane M_{ZG1}. The decrease in BSA rejection at higher ZnO–GO loading (M_{ZG2}) indicates nanoparticle agglomeration, which can create uneven pore structures or localized defects in the membrane. This aggregation may reduce the number of accessible catalytic sites and hinder uniform pollutant contact, potentially lowering the efficiency of DCF removal. In contrast, at the optimal low loading (M_{ZG1}), well-dispersed ZnO–GO provides both enhanced hydrophilicity and a high density of active sites, improving antifouling properties and ensuring effective DCF degradation. Therefore, while M_{ZG2} may maintain moderate permeability, its reduced antifouling performance due to agglomeration could lead to lower photocatalytic efficiency and faster saturation of active sites, ultimately decreasing DCF removal compared to the M_{ZG1} membrane.

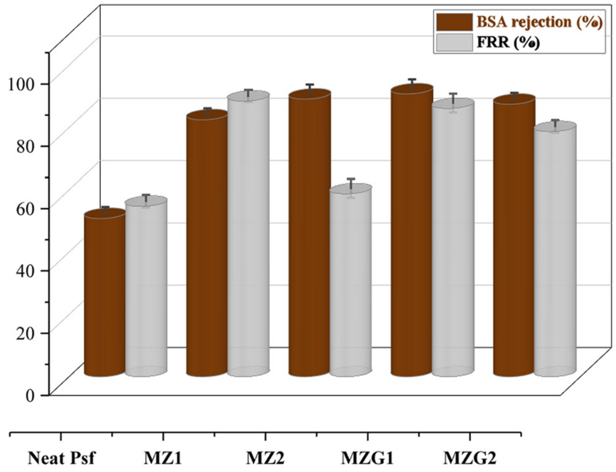

Fig. 13 BSA rejection and flux recovery ratio (FRR) of pristine PSF and nanocomposite membranes.

The presence of ZnO and ZnO–GO nanocomposites in the membranes makes them more hydrophilic and prevents them the adsorption BSA.

The flux recovery ratio (FRR) values of all membranes are higher compared to the pristine PSF membrane (Fig. 13). Elevated FRR values are indicative of enhanced antifouling properties in membranes. The FRR values increased with the presence of ZnO and ZnO–GO nanoparticles at low concentration (0.6 wt%). It is necessary to evidence that the ZnO and GO combination effectively prevented protein adsorption on the membrane surface due to the presence of hydrophilic functional groups.[52] A further increase of the filler concentration caused a slight decrease in the FRR values for the agglomerated formation (reduced hydrophilicity, as also confirmed by contact angle measurements). A lower FRR value was obtained with the PSF membrane due to hydrophobic interactions between PSF and protein molecules.[62]

Previous studies have shown that membranes modified with individual nanoparticles, such as ZnO or GO, exhibit promising degradation efficiency. For instance, PES/ZnO membranes achieved a BSA rejection of 80% and degraded chloride and sulfide compounds between 66–85%.[63] Similarly, PES/GO membranes achieved up to 93% BSA rejection and 84% acridine orange removal.[64] However, these improvements were often hindered by low flux rates and a lack of comprehensive data on long-term operational stability.

Hybrid nanocomposites, such as ZnO–GO, represent a promising solution by combining the synergistic properties of both materials. Mahlangu *et al.* demonstrated 90% organic rejection using PES/ZnO–GO membranes with a moderate water flux of 13.5 L m^{-2} h^{-1} bar^{-1}.[48] In addition, PSF/TiO_2–GO membranes achieved comparable removal performance and low flux (13.05 L m^{-2} h^{-1} bar^{-1}).[65] Although Rosnan *et al.* reported high BSA removal efficiency (98%) using PSF/ZnO–GO membranes with a relatively low water flux of 5.35 L m^{-2} h^{-1} bar^{-1}.[20]

In comparison with earlier studies, this work represents a significant advancement. The PSF/ZnO–GO membrane developed in this study demonstrated a high pure water flux of 19.12 L m^{-2} h^{-1} bar^{-1}, while maintaining excellent pollutant removal efficiencies (91% for BSA (50 mg L^{-1}) and 80% for DCF (25 mg L^{-1})). These results highlight the combined benefits of high permeability and effective contaminant removal, which are crucial for practical water treatment applications. The enhanced performance is attributed to the synergistic interaction between ZnO and GO. ZnO provides photocatalytic activity, while GO improves membrane hydrophilicity, increases pollutant adsorption capacity, and facilitates water transport. Additionally, the consistent performance against various foulants highlights the robustness and multifunctionality of the PSF/ZnO–GO composite membranes. In conclusion, the findings demonstrate that the PSF/ZnO–GO membranes not only match or surpass degradation efficiencies reported in the

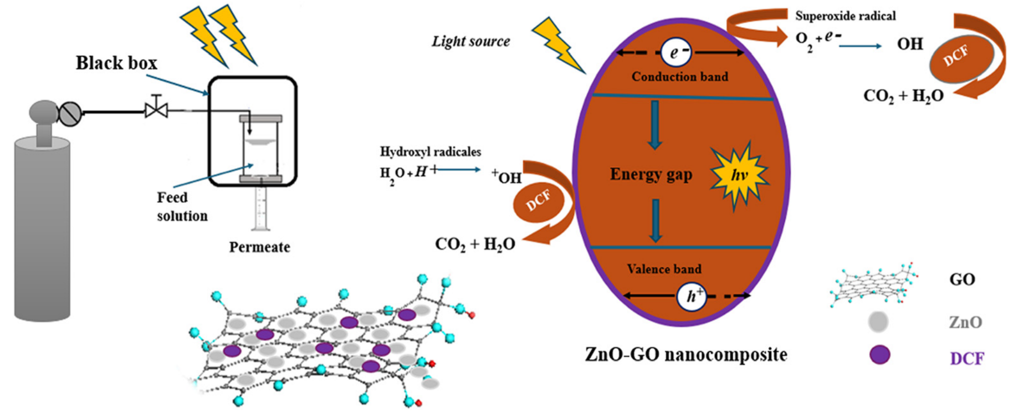

Fig. 14 Photocatalytic mechanism of PSF/ZnO–GO nanocomposite photocatalytic membrane.

literature but also deliver superior water flux and antifouling characteristics. These results confirm the potential of such hybrid nanocomposite membranes for high-performance, durable, and efficient wastewater treatment applications.

Degradation mechanism

The mechanism of DCF degradation under UV light using the synthesized photocatalyst is illustrated in Fig. 14. Under UV irradiation, the activated ZnO–GO nanocomposites lead to the excitation of the electrons and the formation of holes, which facilitate the conversion of water molecules and hydroxyl groups into reactive hydroxyl radicals (·OH).[66] Simultaneously, the electrons in the conduction band react with oxygen to generate additional hydroxyl radicals, which are the key agents in DCF degradation. GO, being a highly conductive material, acts as an excellent electron carrier and transfer medium.[67] This property of GO effectively repels the rapid electron–hole pair recombination typically observed in zinc oxide, which enhances the photocatalytic efficiency.

In fact, electrons in a ZnO's (semiconductor) valence band transition (VB) to the conduction band (CB), creating a hole when exposed to UV light.[68] The photogenerated electrons and holes then reduce and oxidize the organic molecule. In the reaction described below (eqn (11)–(16)), organic wastewater is photocatalytically degraded. The reaction that produces the hydroxyl radical ($OH^{\cdot}$) and superoxide anion ($O_2^{\cdot -}$), which is the primary catalyst for the breakdown of organic materials, is decreased by the e^- in the conduction band (e_{CB}^-). Following hydroxyl radical ($OH^{\cdot}$) decomposition, the organic contaminants in wastewater are mineralized to CO_2 and H_2O.[69]

$$MO_2 + h\nu \rightarrow MO_2(e_{CB}^- + h_{VB}^+)\ \text{M: G, Zn (Photoexcitation)} \tag{11}$$

$$h_{VB}^+ + H_2O \rightarrow H + OH^{\cdot} \tag{12}$$

$$h_{VB}^+ + OH^- \rightarrow OH^{\cdot} \tag{13}$$

$$e_{CB}^- + O_2 \rightarrow O_2^{\cdot -}\ \text{(Reduction in CB)} \tag{14}$$

$$O_2^{\cdot -} + H_2O \rightarrow 2OH_2^{\cdot}\ \text{(Radical generation in CB)} \tag{15}$$

$$OH^{\cdot} + \text{Organic pollutants} \rightarrow CO_2 + H_2O\ \text{(Decomposition)} \tag{16}$$

Performance comparison of PSF–ZnO–GO membrane with other nanocomposite membranes

Several studies have explored the integration of various nanoparticles (NPs) into polymeric membranes to enhance their performance in wastewater treatment. According to the literature, a ZnO/PES membrane achieved notable rejection rates of bovine serum albumin (BSA), chloride (Cl^-), and sulfide (S^{2-}), reaching 80%, 66%, and 85%, respectively.[70] Additionally, a PES/ZnO–GO hybrid membrane achieved 90% rejection of organic compounds,[71] while a PSF/TiO_2–GO membrane displayed rejection efficiencies of 80% for organic contaminants and 90% for ammonia.[65] Particularly promising results have been observed with ZnO–GO nanocomposites embedded in PSF matrices.[20] Rosnan *et al.* showed a pure water flux of 5.35 L m^{-2} h^{-1} bar^{-1}, BSA rejection of 98%, and an FRR of 85%. In the present work, our PSF/ZnO–GO membrane demonstrated superior performance, with a higher pure water flux of 19.12 L m^{-2} h^{-1} bar^{-1} and high rejection rates for both DCF (80%) and BSA (91%), along with an FRR of 86%. These findings underscore the effectiveness of ZnO–GO nanocomposite membranes for the removal of pharmaceutical pollutants, positioning them as a promising candidate for advanced water treatment technologies (Table 4).

Conclusions

ZnO–GO nanocomposites were successfully synthesized *via* a hydrothermal method and incorporated into PSF membranes using the phase inversion technique. The addition of ZnO–GO significantly improved membrane morphology, as confirmed by SEM analysis, which revealed a more porous structure compared to the pristine PSF membrane. This morphological enhancement is attributed to the hydrophilic nature of the nanocomposites. The membrane containing 0.6

Table 4 Comparison of the performance of MMMs membranes blended with various nanoparticles

Nanoparticles (NPs)	Polymer matrix	Pure water flux (L m^{-2} h^{-1} bar^{-1})	Foulant	Degradation rate (%)	FRR (%)	Ref.
ZnO	PES	—	BSA	80	—	70
			Cl^-, S^{2-}	66, 85		
ZnO–GO	PES	—	Organic rejection	90		71
TiO_2/GO	PSF	—	Organic rejection	80	—	65
			Ammonia	90		
ZnO–GO	PSF	5.35	BSA	98	85	20
ZnO–GO	PSF	9.7	DCF	80	86	**Present work**
			BSA	91		

wt% ZnO–GO (M_{ZG1}) exhibited optimal performance, with a notable reduction in water contact angle from 74.7° (pristine PSF) to 51°, resulting in a substantial increase in water flux from 3.7 to 19 L m^{-2} h^{-1} bar^{-1}. Additionally, M_{ZG1} demonstrated superior antifouling properties, with BSA rejection increasing from 51% to 91%, and the flux recovery ratio (FRR) improving from 55% to over 86%.

Under UV-assisted conditions, the M_{ZG1} membrane achieved a DCF removal efficiency of 81%, confirming its photocatalytic activity. Kinetic analysis further indicated that DCF photodegradation followed pseudo-first-order kinetics. These results highlight the potential of the PSF/ZnO–GO membrane as a high-performance, multifunctional ultrafiltration membrane with excellent permeability, antifouling capability, and photocatalytic efficiency, offering excellent performance for the treatment of pharmaceutical contaminants in industrial wastewater.

Author contributions

Zouhair Salah: methodology, investigation, and writing original draft. Hajer Aloulou: methodology, investigation, validation. Saurav Bhattacharyya: methodology, investigation, validation. Veronica Cozzolino: methodology, investigation. Catia Algieri: conceptualization, methodology, investigation, validation, review, and editing. Vincenza Calabrò: validation, project coordinator. Raja Ben Amar: validation, methodology, review, and editing. Sudip Chakraborty: conceptualization, methodology, review.

Conflicts of interest

Authors declare no competing interests.

Data availability

The data that support the findings of this study are available upon request.

Acknowledgements

This work has received funding from the PRIMA Foundation. Grant Agreement number: [2024] [TRUST]-Call 2020 Section 1 Water IA. I would like to thank the Chief Engineer of the Physics Department of the Faculty of Sciences of Sfax, Mrs. DAMMAK Sameh (Sameh.dammak@gmail.com), for carrying out the chemical analyses by FTIR spectroscopy and UV-visible spectroscopy.

References

1 Y. Liu, Z. Yu, X. Li, L. Shao and H. Zeng, *J. Membr. Sci.*, 2021, **617**, 118504.
2 H. Park, J. Barbier and R. P. Hammond, *Solid State Sci.*, 2003, **5**, 565–571.
3 R. Mailler, J. Gasperi, G. Chebbo and V. Rocher, *Waste Manage.*, 2014, **34**, 1217–1226.
4 F. J. Beltrán, P. Pocostales, P. Alvarez and A. Oropesa, *J. Hazard. Mater.*, 2009, **163**, 768–776.
5 G. Z. Kyzas, J. Fu, N. K. Lazaridis, D. N. Bikiaris and K. A. Matis, *J. Mol. Liq.*, 2015, **209**, 87–93.
6 C. I. Kosma, D. A. Lambropoulou and T. A. Albanis, *Sci. Total Environ.*, 2014, **466**, 421–438.
7 N. R. Mirza, R. Huang, E. Du, M. Peng, Z. Pan, H. Ding, G. Shan, L. Ling and Z. Xie, *Desalin. Water Treat.*, 2020, **206**, 83–107.
8 Z. Salah, H. Aloulou, W. Aloulou, C. Algieri, S. M. Chergui and R. Ben Amar, *ChemistrySelect*, 2025, **10**, e202406142.
9 Z. Salah, H. Aloulou, S. Bhattacharyya, C. Algieri and R. Ben Amar, *Euro-Mediterr. J. Environ. Integr.*, 2025, 1–17.
10 N. O. Etafo, M. O. Bamidele, A. Bamisaye and Y. A. Alli, *J. Water Process Eng.*, 2024, **62**, 105369.
11 N. Jallouli, L. M. Pastrana-Martínez, A. R. Ribeiro, N. F. F. Moreira, J. L. Faria, O. Hentati, A. M. T. Silva and M. Ksibi, *Chem. Eng. J.*, 2018, **334**, 976–984.
12 S. Thakur and S. K. Mandal, *New J. Chem.*, 2020, **44**, 11796–11807.
13 T. D. Kusworo, N. Aryanti and F. Dalanta, *IOP Conf. Ser.: Mater. Sci. Eng.*, 2021, **1053**, 012134.
14 W. Raza, M. M. Haque and M. Muneer, *Appl. Surf. Sci.*, 2014, **322**, 215–224.
15 A. Zahid, H. H. Nawaz, A. Siddique, B. Ahmed, S. Razzaque, X. Liu, H. Razzaq and M. Umar, *Mater. Adv.*, 2024, **5**, 9471–9487.
16 R. M. Al-Maliki, Q. F. Alsalhy, S. Al-Jubouri, I. K. Salih, A. A. AbdulRazak, M. A. Shehab, Z. Németh and K. Hernadi, *Membranes*, 2022, **12**, 1043.
17 S. A. Mousa, H. Abdallah and S. A. Khairy, *Sci. Rep.*, 2025, **15**, 2102.
18 S. A. Mousa, H. Abdallah, S. S. Ibrahim and S. A. Khairy, *Appl. Phys. A: Mater. Sci. Process.*, 2023, **129**, 831.

19 T. Pan, Y. Liu, Z. Li, J. Fan, L. Wang, J. Liu and W. Shou, *Sci. Total Environ.*, 2020, **737**, 139818.

20 N. Adilah Rosnan, T. Y. Haan and A. W. Mohammad, *Sains Malays.*, 2018, **47**, 2035–2045.

21 S. Bhattacharyya, L. Donato, S. Chakraborty, V. Calabrò, M. Davoli and C. Algieri, *Earth Syst. Environ.*, 2025, **9**, 639–652.

22 T. D. Kusworo and D. P. Utomo, *J. Environ. Chem. Eng.*, 2017, **5**, 6077–6086.

23 N. Nasrollahi, V. Vatanpour and S. Aber, *J. Water Process Eng.*, 2019, **31**, 100891.

24 J. Yu, Y. Zhang, J. Chen, L. Cui and W. Jing, *J. Membr. Sci.*, 2020, **600**, 117870.

25 N. I. Zaaba, K. L. Foo, U. Hashim, S. J. Tan, W. W. Liu and C. H. Voon, *Procedia Eng.*, 2017, **184**, 469–477.

26 T. Van Khai, L. N. Long, N. H. T. Khoi and N. Hoc Thang, *Crystals*, 2022, 1825.

27 Z. Salah, S. Bhattacharyya, V. Cozzolino, C. Algieri, V. Calabrò, R. B. Amar and S. Chakraborty, *Emergent Mater.*, 2025, **8**, 1671–1685.

28 I. Y. Bouderbala, A. Guessoum, S. Rabhi, O. Bouhlassa and I.-E. Bouras, *Appl. Phys. A: Mater. Sci. Process.*, 2024, **130**, 205.

29 X. Chen, Z. Qu, Z. Liu and G. Ren, *ACS Omega*, 2022, **7**, 23503–23510.

30 D. R. C. Thalayarathna, M. M. D. Samintha, D. Attygalle and D. A. S. Amarasinghe, in *2024 Moratuwa Engineering Research Conference (MERCon)*, IEEE, 2024, pp. 472–476.

31 W. Ma, M. Lv, F. Cao, Z. Fang, Y. Feng, G. Zhang, Y. Yang and H. Liu, *J. Environ. Chem. Eng.*, 2022, **10**, 107840.

32 M. Salavati-Niasari, F. Davar and A. Khansari, *J. Alloys Compd.*, 2011, **509**, 61–65.

33 S. Sivasakthi and K. Gurunathan, *Renewable Energy*, 2020, **159**, 786–800.

34 M. Wojtoniszak and E. Mijowska, *J. Nanopart. Res.*, 2012, **14**, 1–7.

35 M. Naebe, J. Wang, A. Amini, H. Khayyam, N. Hameed, L. H. Li, Y. Chen and B. Fox, *Sci. Rep.*, 2014, **4**, 4375.

36 R. Ahmadi, R. F. Nafchi, P. Sangpour, M. Bagheri and E. Badiei, *Mater. Sci. Eng., B*, 2023, **294**, 116555.

37 S. Kaur and B. Pal, *J. Water Process Eng.*, 2024, **58**, 104765.

38 F. Khan, M. S. Khan, S. Kamal, M. Arshad, S. I. Ahmad and S. A. A. Nami, *J. Mater. Chem. C*, 2020, **8**, 15940–15955.

39 A. Ramesh, P. Tamizhdurai, P. S. Krishnan, V. K. Ponnusamy, S. Sakthinathan and K. Shanthi, *Fuel*, 2020, **262**, 116494.

40 J. T. Jung, J. F. Kim, H. H. Wang, E. Di Nicolo, E. Drioli and Y. M. Lee, *J. Membr. Sci.*, 2016, **514**, 250–263.

41 L. Y. Ng, A. W. Mohammad, C. P. Leo and N. Hilal, *Desalination*, 2013, **308**, 15–33.

42 L. Yan, Y. S. Li, C. B. Xiang and S. Xianda, *J. Membr. Sci.*, 2006, **276**, 162–167.

43 S. I. Voicu, M. A. Pandele, E. Vasile, R. Rughinis, L. Crica, L. Pilan and M. Ionita, *Dig. J. Nanomater. Biostruct.*, 2013, **8**, 1389–1394.

44 J. Kavitha, M. Rajalakshmi, A. R. Phani, P. Sherugar and M. Padaki, *Int. J. Environ. Sci. Technol.*, 2023, **20**, 10031–10048.

45 P. V. Viotti, W. M. Moreira, O. A. A. dos Santos, R. Bergamasco, A. M. S. Vieira and M. F. Vieira, *J. Cleaner Prod.*, 2019, **219**, 809–817.

46 H. Wang, W. Wang, L. Wang, B. Zhao, Z. Zhang, X. Xia, H. Yang, Y. Xue and N. Chang, *Chem. Eng. J.*, 2018, **334**, 2068–2078.

47 D. Sen, A. K. Ghosh, S. Mazumder, R. C. Bindal and P. K. Tewari, *Sep. Purif. Technol.*, 2014, **123**, 79–86.

48 O. T. Mahlangu, R. Nackaerts, B. B. Mamba and A. R. D. Verliefde, *Water Sci. Technol.*, 2017, **76**, 501–514.

49 K. C. Ho, Y. H. Teow, W. L. Ang and A. W. Mohammad, *Sep. Purif. Technol.*, 2017, **177**, 337–349.

50 H. Rabiee, V. Vatanpour, M. H. D. A. Farahani and H. Zarrabi, *Sep. Purif. Technol.*, 2015, **156**, 299–310.

51 F. Kazemi, Y. Jafarzadeh, S. Masoumi and M. Rostamizadeh, *J. Environ. Chem. Eng.*, 2021, **9**, 104992.

52 Y. T. Chung, E. Mahmoudi, A. W. Mohammad, A. Benamor, D. Johnson and N. Hilal, *Desalination*, 2017, **402**, 123–132.

53 A. N. Tuama, L. H. Alzubaidi, M. H. Jameel, K. H. Abass, M. Z. H. B. Mayzan and Z. N. Salman, *J. Sol-Gel Sci. Technol.*, 2024, **110**, 792–806.

54 C. Ding, X. Qin, Y. Tian and B. Cheng, *J. Membr. Sci.*, 2022, **659**, 120789.

55 M. Pavel, C. Anastasescu, R.-N. State, A. Vasile, F. Papa and I. Balint, *Catalysts*, 2023, **13**, 380.

56 P. Mathumba, K. Maziya, A. T. Kuvarega, L. N. Dlamini and S. P. Malinga, *Water SA*, 2020, **46**, 500–505.

57 F. Güzel and F. Koyuncu, *Biomass Convers. Biorefin.*, 2023, **13**, 2401–2412.

58 G. Moradi, M. Rahimi and S. Zinadini, *J. Environ. Chem. Eng.*, 2021, **9**, 104717.

59 M. Alhoshan, J. Alam, A. K. Shukla and A. A. Hamid, *J. Mater. Res. Technol.*, 2023, **24**, 6034–6047.

60 S. Mondal and S. K. Majumder, *Chem. Eng. J.*, 2020, **401**, 126036.

61 S. Ahmadipouya, S. A. Mousavi, A. Shokrgozar and D. V. Mousavi, *J. Environ. Chem. Eng.*, 2022, **10**, 107535.

62 N. Baig, A. Matin, M. Faizan, D. Anand, I. Ahmad and S. A. Khan, *J. Environ. Chem. Eng.*, 2022, **10**, 108166.

63 T. D. Kusworo, N. Aryanti, Q. Qudratun, V. D. Tambunan and N. R. Simanjuntak, *J. Teknol.*, 2018, **80**, 9–15.

64 A. Abdel-Karim, S. Leaper, M. Alberto, A. Vijayaraghavan, X. Fan, S. M. Holmes, E. R. Souaya, M. I. Badawy and P. Gorgojo, *Chem. Eng. J.*, 2018, **334**, 789–799.

65 T. D. Kusworo, H. Susanto, N. Aryanti, N. Rokhati, I. N. Widiasa, H. Al-Aziz, D. P. Utomo, D. Masithoh and A. C. Kumoro, *J. Environ. Chem. Eng.*, 2021, **9**, 105066.

66 K. S. Ranjith, P. Manivel, R. T. Rajendrakumar and T. Uyar, *Chem. Eng. J.*, 2017, **325**, 588–600.

67 A. A. Yaqoob, N. H. binti Mohd Noor, A. Serra and M. N. Mohamad Ibrahim, *Nanomaterials*, 2020, **10**, 932.

68 S. A. Yaqoob, N. H. binti Mohd Noor, A. Serrà, M. Nasir and M. Ibrahim, *Nanomaterials*, 2020, **10**, 932.

69 S. A. Al-Zahrani, A. M. Khedr, A. M. Alturki and W. S. A. El-Yazeed, *J. Mol. Liq.*, 2024, **395**, 123956.

70 T. D. Kusworo, D. Soetrisnanto, N. Aryanti, D. P. Utomo, V. D. Tambunan and N. R. Simanjuntak, *J. Water Process Eng.*, 2018, **23**, 239–249.

71 O. T. Mahlangu, R. Nackaerts, J. M. Thwala, B. B. Mamba and A. R. D. Verliefde, *J. Membr. Sci.*, 2017, **524**, 43–55.